A Minimally Invasive Robotic Tissue Palpation Device

Mohammad Mir ⓘ, Jiawen Chen ⓘ, Aneri Patel ⓘ, Meghan R. Pinezich ⓘ, Brandon A. Guenthart ⓘ, Gordana Vunjak-Novakovic ⓘ, and Jinho Kim ⓘ

Abstract—*Objective:* **Robot-assisted minimally invasive surgery remains limited by the absence of haptic feedback, which surgeons routinely rely on to assess tissue stiffness. This limitation hinders surgeons' ability to identify and treat abnormal tissues, such as tumors, during robotic surgery.** *Methods:* **To address this challenge, we developed a robotic tissue palpation device capable of rapidly and non-invasively quantifying the stiffness of soft tissues, allowing surgeons to make objective and data-driven decisions during minimally invasive procedures. We evaluated the effectiveness of our device by measuring the stiffness of phantoms as well as lung, heart, liver, and skin tissues obtained from both rats and swine.** *Results:* **Results demonstrated that our device can accurately determine tissue stiffness and identify tumor mimics. Specifically, in swine lung, we determined elastic modulus (E) values of 9.1 $\pm$ 2.3, 16.8 $\pm$ 1.8, and 26.0 $\pm$ 3.6 kPa under different internal pressure of the lungs (PIP) of 2, 25, and 45 cmH$_2$O, respectively. Using our device, we successfully located a 2-cm tumor mimic embedded at a depth of 5 mm in the lung subpleural region. Additionally, we measured E values of 33.0 $\pm$ 5.4, 19.2 $\pm$ 2.2, 33.5 $\pm$ 8.2, and 22.6 $\pm$ 6.0 kPa for swine heart, liver, abdominal skin, and muscle, respectively, which closely matched existing literature data.** *Conclusion/Significance:* **Results suggest that our robotic palpation device can be utilized during surgery, either as a stand-alone or additional tool integrated into existing robotic surgical systems, to enhance treatment outcomes by enabling accurate intraoperative identification of abnormal tissue.**

Index Terms—**Robot-assisted minimally invasive surgery, tactile feedback, tissue palpation, tissue stiffness, tumor removal.**

Mohammad Mir, Jiawen Chen, and Aneri Patel are with the Department of Biomedical Engineering, Stevens Institute of Technology, USA.

Meghan R. Pinezich is with the Department of Biomedical Engineering, Columbia University, USA.

Brandon A. Guenthart is with the Department of Cardiothoracic Surgery, Stanford University, USA.

Gordana Vunjak-Novakovic is with the Department of Biomedical Engineering and Medicine, Columbia University, USA.

Jinho Kim is with the Department of Biomedical Engineering, Stevens Institute of Technology, Hoboken, NJ 07030 USA (e-mail: jkim6@stevens.edu).

I. INTRODUCTION

ROBOT-ASSISTED minimally invasive surgery (RMIS) has emerged as an approach that allows surgeons to perform complicated surgical procedures with improved dexterity, visualization, and precision and accuracy that can collectively enhance treatment outcomes [1], [2]. Advanced robotic surgical systems, such as the da Vinci system (Intuitive Surgical, Inc.) and Senhance Surgical System (TransEntrix Inc.), offer multiple advantages, including increased degrees of freedom, high-definition visualization of the surgical site with accurate depth perception, and enhanced scalability [3]. RMIS performed using these surgical systems provides unique benefits to patients, including reduced pain and discomfort, smaller incisions, minimal blood loss, and faster recovery time [4]. Accordingly, RMIS is becoming increasingly used for a wide range of specialties, including thoracoscopic, hepatobiliary, gynecologic, urologic and gastrointestinal surgery [5].

Despite the numerous advantages and benefits, one of the widely recognized limitations of RMIS is the absence of tactile sensations (i.e., touch- and force-related sensations) [6]. During traditional open surgery, surgeons often use tactile feedback through manual palpation to examine the pathologic conditions of the tissues [7]. In particular, because pathologic tissues, such as tumors [8] and fibrosis [9], are stiffer than normal tissues, intra-operative manual palpation enables surgeons to identify diseased tissues that must be surgically treated. However, during RMIS, surgeons rely on visual information to assess the tissues because the use of robot arms for surgical operation limits their ability to receive tactile feedback [10].

One potential solution to overcoming the loss of tactile perceptions during RMIS is to remove tissue from the organ and evaluate the biological, mechanical, or physiological characteristics of the removed tissue through conventional assays, such as immunostaining, tensile testing, and gene profiling [11], [12]. While the *ex vivo* measurements can provide detailed insight into the molecular and cellular characteristics of the tissues, they are slow and destructive as tissue removal is required for the downstream analyses. Further, the accuracy of measurements

may be compromised as the native microstructure and biological properties of the tissues can change when removed from the body. Pre-operative imaging-based analysis modalities, such as computed tomography (CT), magnetic resonance imaging (MRI), and elastography, can allow rapid and non-destructive determination of tissue structure and properties. However, these imaging modalities remain limited by their special resolution and only provide a single historical snapshot which is often difficult for the surgeon to utilize in real-time during an operation [13], [14].

Since mechanical properties of tissue are often associated with tissue state and pathology [15], several studies have investigated quantitative tissue stiffness assessment using mechanical palpation approaches, including rolling indentation [16], [17], [18], vertical indentation [19], [20], [21], [22], vibration [23], grasping [24], [25], and sweeping [26]. Typically, the palpation devices incorporate tactile sensors [27], such as electrical-based and optical-based sensors, to obtain force- and touch-related information. By applying deformation on the tissue surface and measuring the resulting forces, tissue stiffness can be quantified through mathematical modeling of the force-deformation relationship. Such devices have been useful in generating high-resolution stiffness distribution maps of tissues, which have effectiveness in localizing tumors in *ex vivo* [16], [28] and *in vivo* [19], [21] cancer models. Further, few studies have explored a combinative approach using quantitative analyses and experimental palpation to determine the viscoelastic properties of healthy and pathological tissues [22], [29].

The size, sensitivity, and sterilizability of the measurement probe are key factors considered in the development of palpation devices for RMIS. To minimize the required space for intraoperative application of a palpation device, few studies have developed wireless and Bluetooth-based palpation probes [21], [30], while several studies have explored the incorporation of the palpation mechanism into existing surgical tools, such as endoscopes [29], [31], robotic arms [19], [32], and surgical forceps [24], [25], [33]. Notably, both approaches allow for the deployment of the probe through the RMIS trocar port, facilitating intraoperative stiffness measurements. Additionally, integrating the palpation probes into surgical tools can reduce the time required for surgeons' training [33]. Moreover, the sensitivity of the palpation probe is a crucial design factor, as a highly sensitive probe allows precise identification of tumor margins that must be surgically resected and the detection of anatomical structures, such as nerves and blood vessels, that must be avoided during surgical procedures [21]. Furthermore, a number of palpation devices are designed to be either sterilizable [31] or disposable [34], [35] to align with the clinical requirements.

In this study, we present a robotic tissue palpation device that can accurately, rapidly, and minimally invasively quantify tissue stiffness during RMIS by determining elastic modulus (E) *in situ* (Fig. 1(a) and (b)). Notably, the measurement probe in our device incorporates a novel electrical-based sensing method to monitor the predefined tissue deformation. Existing palpation probes utilize optical [16], [20], mechanical [21], [36], or computer-assisted [17], [19], [22], [28] techniques to determine tissue deformation. Within our probe's design, two contact electrodes are integrated adjacent to the sensor head (i.e., hemispheric indenter) to provide real-time feedback on the maximum predefined deformation (Fig. 1(c) and (d)). To the best of our knowledge, the use of contact electrodes to indicate resulting predefined deformation has not been previously demonstrated. We constructed the device and tested its functionality of the device prototype by measuring the stiffness of tissue mimics and biological tissues obtained from animal models. The measurement accuracy and reproducibility were confirmed by comparing the readouts with the values reported in the literature. Our device was able to accurately locate tumor mimetics in cancer models. Collectively, we confirmed that our device has the great potential to provide an accurate and objective tissue stiffness assessment that can ultimately allow surgeons to detect and treat pathologic tissues, such as small tumors, during robotic surgery.

II. MATERIALS AND METHODS

A. Overview of the Robotic Tissue Palpation Device

The robotic tissue palpation device has been designed to intra-operatively and non-destructively quantify the stiffness of soft tissues (e.g., lung, heart, and liver) by measuring the elastic modulus of the tissue (Fig. 1(a)). The measurement sensor probe incorporated into the distal end of the catheter consisted of a thin force sensor, a rigid hemispheric indenter head, two contact electrodes, and an imaging probe (Fig. 1(b) and (c)). To determine the tissue stiffness, the probe was directed downward perpendicular to the tissue surface (Fig. 1(d), i). A force was then continuously applied against the tissue surface at a rate of 5 mm/min via the hemispheric indenter to compress the tissue. Predefined magnitude of tissue deformation, which was determined by the height of the indenter (i.e., 2 mm), was confirmed when the electrical signal was detected across the two contact electrodes (Fig. 1(d), ii). Subsequently, the elastic modulus of the tissue was calculated by correlating the magnitude of the compression force (F_C) and the deformation length of the tissue (L_C) using Hertz's equation developed for spherical indentation:

$$E = \frac{3}{4} \frac{F_C \left(1 - \nu^2\right)}{L_C^{3/2} r^{1/2}} \tag{1}$$

where E is the elastic modulus of the tissue, F_C is the force measured by force sensor at maximum deformation, L_C is the maximum deformation, υ is Poisson's ratio, and r is the radius of the hemispheric indenter (Supplementary Methods). The Poisson's ratio was assumed to be 0.5 for the tissue phantoms and the biological tissues [37]. A single indentation was performed against the tissue surface for each measurement.

B. Palpation Device Design and Construction

The device consisted of three key components: *i*) a deployable sensing probe mounted on a steerable catheter that can compress local tissue for stiffness measurement, *ii*) a motion control module that enables multi-directional device movements, such as linear displacement, rotation, and deflection of the device,
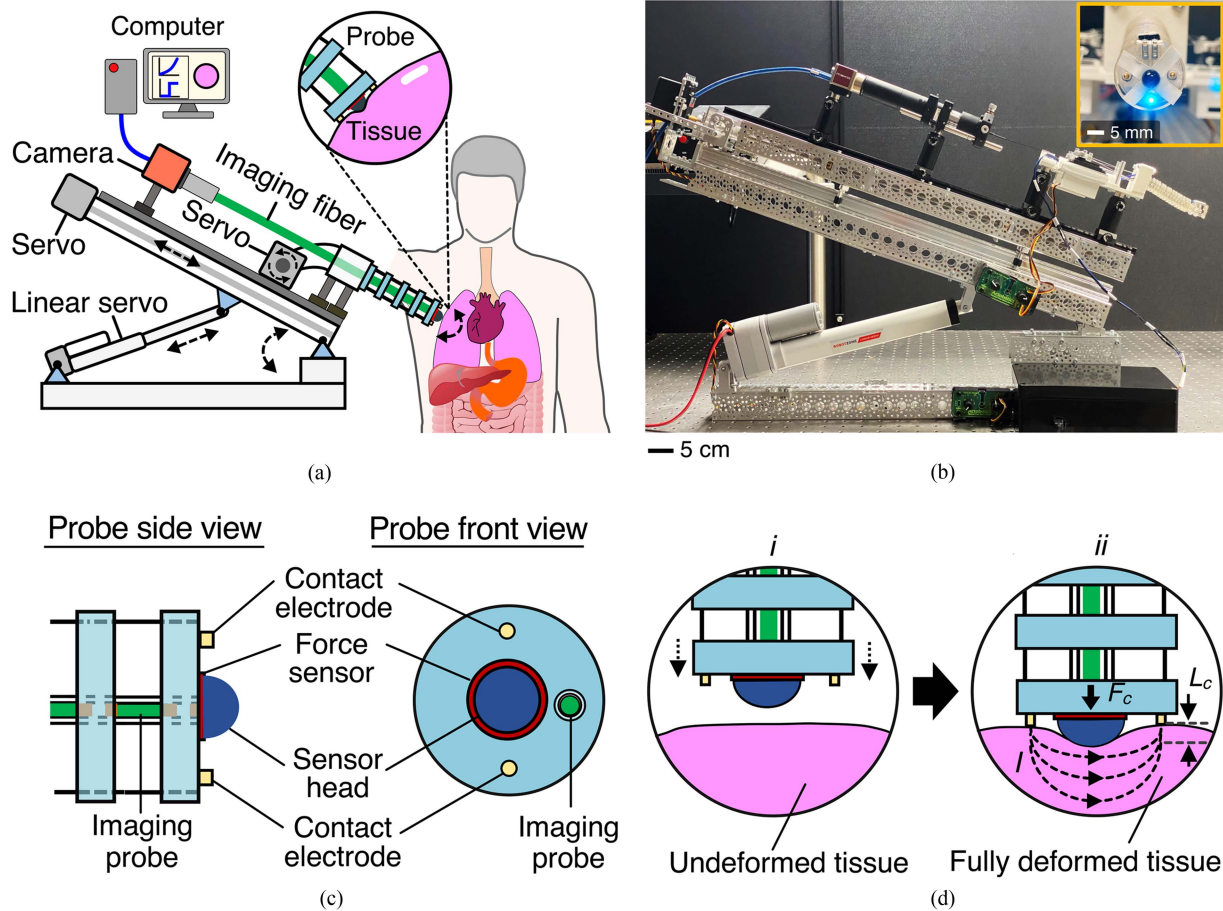
Fig. 1. Overview of the robotic tissue palpation device. (a) A schematic showing the application of the device in measuring the stiffness of soft biological tissues. The device consists of a stiffness measurement probe positioned at the distal end of the deflectable catheter, an imaging fiber integrated into the device for visual guidance during device operation, and a motorized controller for manipulating the spatial orientation of the device during navigation and measurement. (b) A photograph of the robotic palpation device. Inset image: magnified front view of the measurement probe. (c) A schematic showing the components of the measurement probe: contact electrodes to confirm probe-tissue contact and maximum tissue deformation, force sensor to measure the force applied to the tissue during measurement, and imaging probe to provide visual information during device navigation and stiffness measurement. (d) A schematic showing i) undeformed tissue and (ii) and fully deformed tissue (L_C: tissue deformation length) under applied force (F_C). Maximum tissue deformation is confirmed when the flow of electrical current (I) is generated across the tissue between the contact electrodes integrated at the device distal end.

and *iii*) a micro-optical imaging module that provides the visual information during the probe navigation and tissue stiffness measurement.

C. Stiffness Measurement Sensing Probe

The stiffness measurement sensing probe consisted of a thin film-based force sensor (diameter: 3 mm; GD03-10N, UNEO), two spiral-headed pogo pins as contact electrodes (diameter: 1 mm, MilMax), and a rigid hemispheric compression head made of acrylic plastic (height: 2 mm). To utilize the force sensor in the stiffness measurement application, a force-to-voltage circuit was created using a digital data acquisition device (Arduino UNO, Rev 3), a reference resistor (R, Microchip), and custom-written MATLAB code (MATLAB R2021). In addition, an electrical circuit was formed between the contact electrodes (i.e., pogo pins) to quantify tissue deformation through acquisition of voltage as the readouts.

The steerable catheter arm was designed as a wire-driven continuum robot and constructed with driving disks, driving wires, and flexible tubing. The robotic catheter was integrated into the tissue palpation device via a 3D printed adapters made of poly(lactic acid) (PLA; MakerBot), which was mounted on the device using dovetail rail carriers and a dovetail optical rail. A complete description of the measurement probe, the deflectable catheter, and the electrical/optical circuits is provided in the Supplementary Methods.

D. Device Movement Control

Deflection, tilting, and linear displacement movements were enabled in the device to guide the measurement probe to the target tissue surface (Fig. 2, Fig. S1). The movement control module consisted of a linear motor (HDLS-8-50-12V, Robotzone) that controlled the tilting movement, a servo motor (HS-785HB, HITEC RCD) that modulates the translational movement, and

Deflection movement — 1 cm — (a)

Tilting movement — 5 cm — (b)

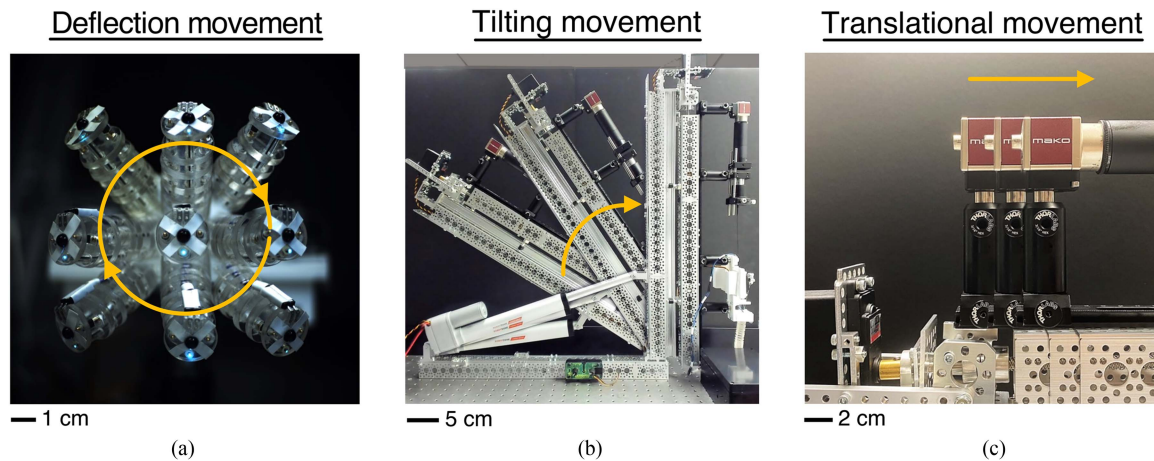**Translational movement** — 2 cm — (c)

Fig. 2. Multi-directional movements of the robotic tissue palpation device. Multiplicity photographs illustrating (a) deflection, (b) titling, and (c) translational movements of the device accomplished through manipulation of individual motors integrated into the device. During device operation, these movements are collectively achieved by simultaneously controlling different motors to bring the distal end of the device to the tissue surface for the stiffness measurement.

two high-precision servo motors (HS-311, HITEC RCD) that control the deflection movements of the catheter's distal end. During the device operation, all the motors were controlled simultaneously using two motor controllers (605105, Acrobatics).

The deflection movement of the catheter arm was enabled by a wire-driven conformation that allowed multi-angular movements of the device tip in three-dimension (3D) space (Fig. 2(a), Fig. S2, Movie S1). The desirable probe deflection was achieved by pushing and pulling the driving wires via pulleys, mounted on servo motors. Tilting movement was enabled by extending or retracting a linear servo integrated into the device (Fig. 2(b)). Specific tilting motions of the device could be achieved by adjusting the length of the linear servo arm (Movie S2). Furthermore, a servo motor was installed on the back of the rail to control the linear motion of the measurement probe (Fig. 2(c), Movie S3).

E. Fiber-Optic Imaging Module

A custom-built imaging module was integrated into the tissue palpation device that allowed vision-assisted navigation during device operation and tissue stiffness measurements (Fig. 3(a)). The imaging module consisted of an LED illumination light source (M565L3, Thorlabs), a flexible optical-fiber imaging bundle with embedded SELFOC micro-lens (FIGH-30-650S, Fujikura), a monochrome CMOS camera (Mako, Allied Vision), an achromatic doublet (tube lens; AC254-150-A-ML, Thorlabs), a 10× objective lens (Olympus), a filter holder (STK01, Thorlabs), a fiber bundle adapter (S120-SMA, Thorlabs), a translating lens mount (CXY1, Thorlabs), and extension tubes (Thorlabs).

For imaging an object, such as an organ, the distal end of the imaging fiber bundle (i.e., imaging tip) was introduced into the imaging channel of the catheter, and the image formed on the proximal end passed through the objective lens and collected by the camera's imaging sensor (Fig. 3(b) and (c)). The resolution
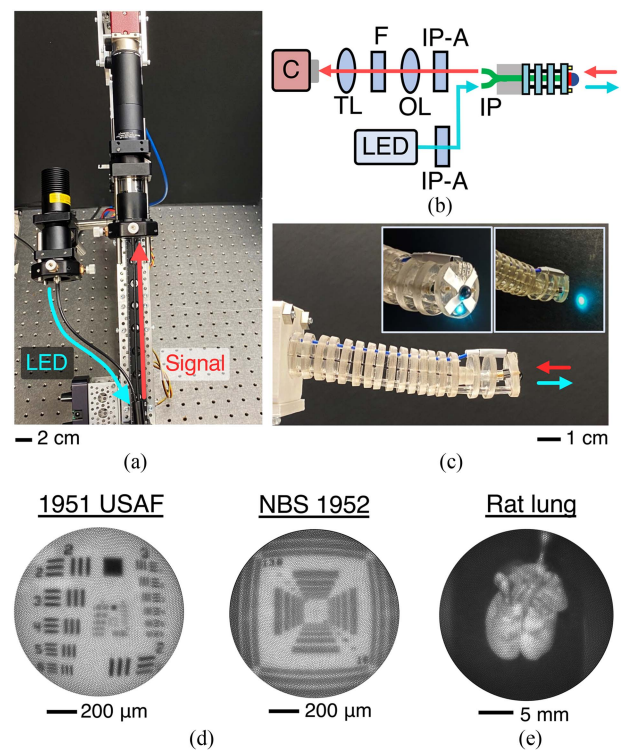

Fig. 3. Custom-built micro-optical imaging module. The imaging module for collecting visual information in bright-field and fluorescence imaging modes to guide the device for tissue assessment. (a) A photograph of the imaging module integrated into the palpation device and (b) light-path schematic of the imaging module. C: camera, LED: light-emitting diode, TL: tube lens, F: filter, OL: objective lens, IP-A: imaging probe adapter, IP: imaging probe. (c) A photograph showing the distal end of the palpation device incorporated with an optical fiber-based imaging probe. Inset images: excitation/illumination lights being emitted through the distal end of the imaging probe. (d) 1951 USAF and NBS 1952 test targets imaged using the imaging module showing the resolution of 80 mm/line and 72 mm/line, respectively. (e) A photograph of an explanted rat lung taken using the imaging probe positioned approximately 5 cm away from the lung.
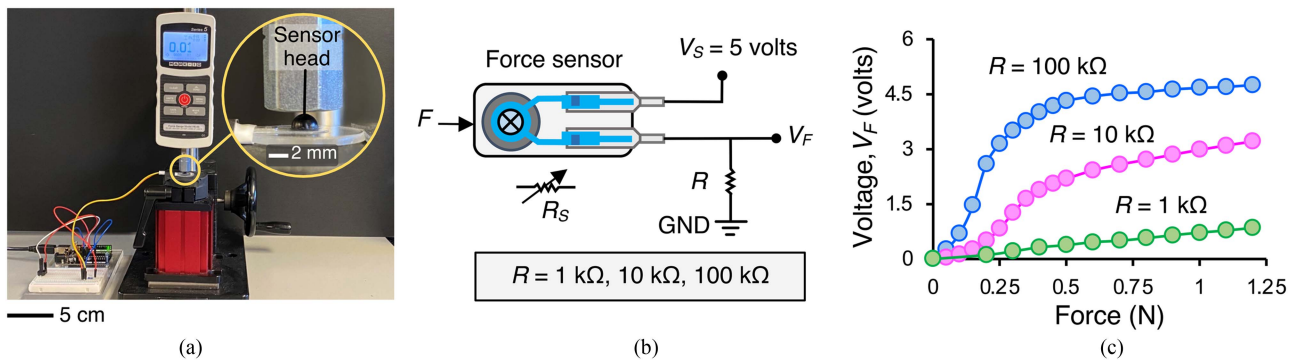
Fig. 4. Force sensor circuit construction and calibration. (a) A photograph illustrating the experimental setup used to calibrate the thin film-based force sensor (GD03-10N, UNEO) used to construct the palpation device. Known magnitudes of compression force were applied directly to the force sensor incorporated underneath the hemispheric indentation head using a commercial force meter (M5-2 force gauge). Changes in the voltage were recorded to calibrate the force sensor. (b) A schematic of the electrical circuit to construct and calibrate the force sensor against different resistor incorporated (R: 1, 10, or 100 kΩ). (c) Voltage values measured from the force sensor against the compression force applied during the measurement. The circuit incorporated with a 100-kΩ resistor showed greater sensitivity at the force range of 0-0.5 N, as the changes in the voltage against the compression force was more drastic. This led to the use of a 100-kΩ resistor to construct the palpation device for the stiffness measurements conducted using soft phantoms and tissue in this study. F: force, R: reference resistor, R_S: the resistance between force sensor conductive layers, GND: ground, V_S: supply voltage.

of the imaging module was approximately 80 μm/line pair (one light line and one dark line) and 74 μm/line pair for USAF 1951 and NBS 1951 targets, respectively, at 1 mm working distance (Fig. 3(d) and Supplementary Methods). Using this imaging module, we obtained bright-field images of entire structure as well as smaller tissue regions of the *ex vivo* rat lungs (Fig. 3(e), Fig. S3) and rat liver (Fig. S3).

F. Force Sensor Circuit and Calibration

Prior to all stiffness measurements, the force sensor circuit was calibrated by measuring the output voltages against known forces applied to the sensor using a force gage (M5-2, Mark-10) (Fig. 4(a)). The circuit consisted of a digital data acquisition device (Arduino UNO, Rev 3), a reference resistor (R, Microchip), and custom-written MATLAB code (MATLAB R2021) The output voltage (V_F) versus force load (F) curves were generated for all resistors (force range: 0-5N) (Fig. 4(b)). Different reference resistors (R; 1, 10, and 100 kΩ) integrated into the sensor circuit to investigate the role of the resistance on the measurement outcomes (Fig. 4(b) and (c)). The measurements showed that increasing the value of reference resistance increased the sensitivity of the force measurement at lower force range (below 0.5 N). Since lung and liver tissues are soft, the 100 kΩ-resistor was used for the stiffness measurements (Fig. 4(c)).'

G. Fabrication of Tissue Phantoms

Gelatin-based tissue phantoms were prepared by dissolving gelatin powder (G2500, Sigma-Aldrich) in 1× phosphate-buffered saline (1× PBS; Gibco) at 70 °C (concentration: 5, 10, and 15%) and physically crosslinking the solutions at 4 °C for 30 min. All tissue phantoms were left at room temperature for 30 minutes prior to stiffness measurements. To create tissue phantom with spatially heterogenous stiffness, a cylindrical Indocyanine Green (ICG)-labeled poly(dimethylsiloxane) (PDMS) (ratio of prepolymer to crosslinker: 10:1; diameter: 12 mm,

thickness: 2.5 mm) was embedded at the center of a gelatin block (concentration: 10% w/v; length: 35 mm, width: 35 mm, thickness: 10 mm). The details of the preparation method are provided in the Supplementary Methods.

H. Rat and Swine Organ Harvest

Lungs and livers were obtained from Sprague-Dawley rats (SAS SD rats; total: 6 rats; weight: 250–270 g; Charles River Laboratories). All animal care, handling, and experimental work were conducted under the animal protocol approved by the Stevens Institute of Technology Institutional Animal Care and Use Committee (IACUC). A complete description of the animal experiment procedure is provided in the Supplementary Methods. Briefly, animals were euthanized, and lungs and livers were isolated and rinsed with 1×PBS prior to the stiffness measurements. Lungs were ventilated for 10 min with a tidal volume of 2.2 mL to eliminate the variations that could be caused by inflation and deflation history.

Further, freshly isolated swine organs, including lungs, heart, liver, and abdominal skin and muscle (ventral region), were purchased from a local slaughterhouse (Dealaman Enterprise, Warren, NJ). The stiffness measurements of all organs were conducted on the day of harvesting. To minimize the variability between the lungs resulting from different inflation and inhalation histories, the swine lungs were ventilated with a manual resuscitator (Ambu bag) connected to a pressure sensor for 10 min.

I. Lung Cancer Model

To produce an *ex vivo* lung cancer (tumor) model, an incision was made in the distal region of the swine lung using a blade, and an ICG-labelled PDMS (diameter: 2 cm; thickness: 5 mm) that mimics a nodule was inserted into the subpleural region, approximately 5 mm below the pleura surface. The incised area was then sutured (4-0 silk) to prevent air leak and lung collapse.
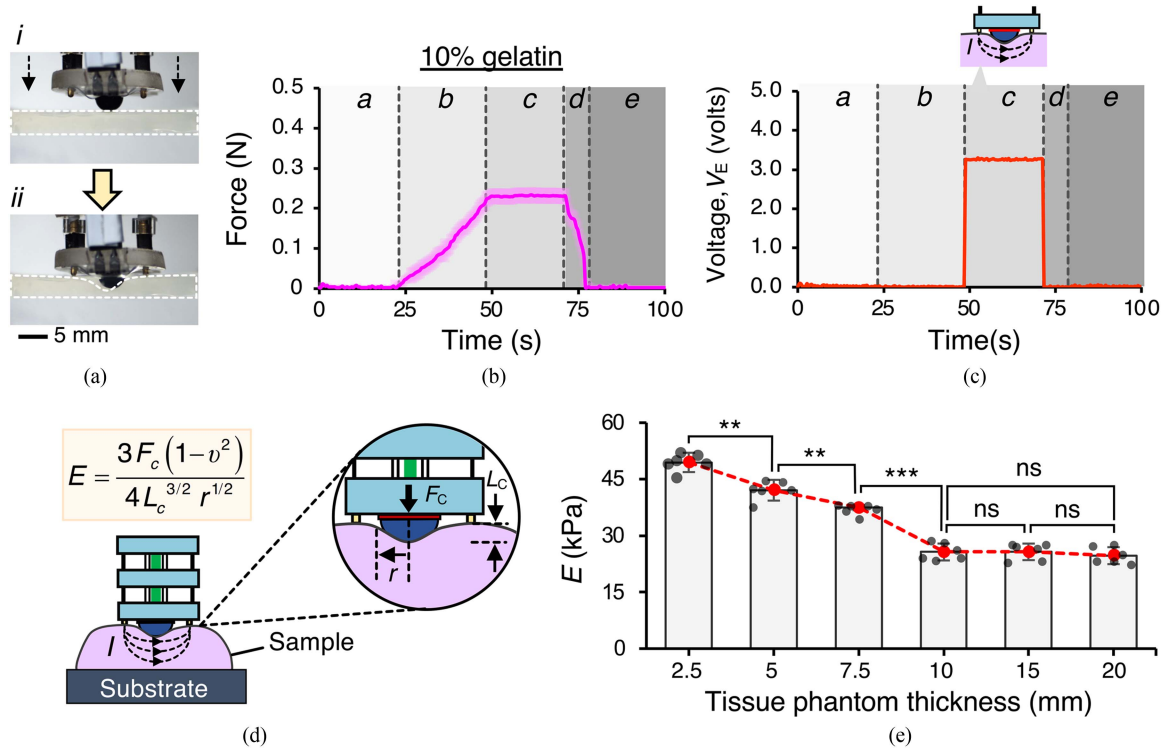
Fig. 5. Stiffness evaluation of gelatin-based tissue phantoms. (a) Photographs showing: *i)* no contact and *ii)* full contact established between the tissue phantom and contact electrodes. In this configuration, a predefined deformation of a phantom or tissue is confirmed when an electrical current flows between the two contract electrodes, indicating the circuit has been closed due to the full contact between the electrodes with phantom or tissue. (b) A plot showing the force recorded over time as phantoms made of 10% v/w gelatin were being compressed using the device (rate of deformation: 5 mm/min). Region *a*: The probe approaching the phantom surface for measurement. Region *b*: The probe making a contact with the phantom and deforming it up to 2 mm ($L_C = 2$ mm), which is equivalent to the height of the hemispherical compression head. Region *c*: No further compression induced due to full contact between the electrodes and phantom. Region *d*: The probe being retracted following the measurement. Region *e*: Complete detachment of the probe from the phantom as no force was being recorded. (c) Voltage (V_E) recorded via the contact electrodes during the experiment. Maximum deformation (i.e., Region *c*) was confirmed when the electrical circuit is closed, which was indicated by 3.2 volts of V_E measured. (d) A schematic showing the deformation of tissue sample (L_C: deformation length) under applied force (F_C) and the equation formulated to calculate the elastic modulus (E). *r*: radius of sensor indentation head, ν: Poisson ratio. (e) Demonstration of elastic modulus (E) measurements using phantom blocks ($n = 6$, gelatin concentration: 10%) with different thicknesses (2.5–20 mm) that were placed on a rigid acrylic substrate (E: ~3.1 GPa). As the phantom thickness increased, the measured E values decreased due to reduced effects of the substrate located underneath the phantom samples ($**p$-value < 0.01. $***p$-value < 0.001. ns: not significant).

J. Study Design and Statistical Analysis

All experimental data were presented as mean ± standard deviation (SD). All experiments were performed at least five times (n > 5; n: number of samples) to ensure reproducibility and to evaluate statistical significance between experimental groups. One-way analysis of variance (One-way ANOVA) was performed, followed by Tukey's honest significant *post hoc* test to compare different groups. A difference was considered statistically significant when $p < 0.05$.

III. RESULTS

A. Measurements of Tissue Phantom Stiffness

To evaluate the functionality and measurement accuracy of the palpation device, we evaluated the stiffness of gelatin-based tissue phantoms (Fig. 5). The phantoms were compressed using the measurement probe while the deformation was continuously monitored using a camera (Fig. 5(a)). To determine the elastic modulus, the sensor head was gently pushed against the tissue phantom while the applied force was being recorded continuously (Fig. 5(b), region *b*). The tissue deformation continued until the tip of both contact electrodes touched the tissue surface due to maximum tissue deformation (i.e., 2 mm). The contact between tissue and electrodes was confirmed by detecting an electrical signal as the electrical circuit between the contact electrodes was closed (Fig. 5(c), Fig. S4). When the maximum deformation was achieved, the voltage (V_E) recorded during the measurement showed a step response of 3.2 volts (Fig. 5(c), region *c*). The E values were then calculated based on the maximum deformation length (L_C: 2 mm) and the corresponding force measured (F_C) using an equation developed for spherical indenters (Fig. 5(d) and Supplementary Methods).

The rigid substrate made of an acrylic plastic (8473K112, McMaster, E: ~3.1 GPa), onto which tissue mimics or tissue samples were placed could influence the stiffness readouts in indentation-based measurements [38]. Accordingly, we evaluated the stiffness of gelatin tissue phantoms (concentration: 10% w/v) of different thicknesses (2.5, 5, 7.5, 10, 15, and 20 mm) to find the critical tissue thickness at which the effect of the
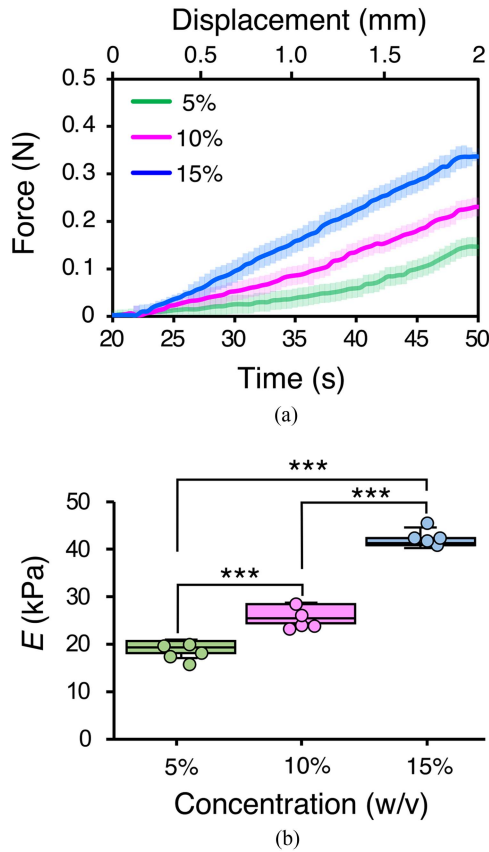
Fig. 6. Stiffness evaluation of gelatin-based tissue phantoms with varying gelatin concentrations using the palpation device. (a) Magnitude of the force measured continuously as the phantoms were compressed at a compression rate of 5 mm/min. Shaded regions indicate standard deviations. The slope of the force-displacement curve increased with an increase in gelatin concentration. (b) Elastic moduli of the phantoms calculated using the maximum deformation and force recorded during the measurements. Higher gelatin concentration was correlated with a higher elastic modulus. For 5, 10, and 15% w/v gelatin phantoms, the measured elastic moduli were 18.3 ± 1.5, 25.7 ± 2.2, and 42.5 ± 1.6 kPa, respectively (***p-value < 0.001).

substrate is negligible (Fig. 5(e)). The measured E values were 49.5 ± 2.6, 42.1 ± 2.8, 37.4 ± 0.7, 25.7 ± 2.3, 25.7 ± 2.2, and 24.5 ± 2.3 kPa for phantoms with the thickness of 2.5, 5, 7.5, 10, 15, and 20 mm, respectively. These results show that the effect of substrate on the measured stiffness decreased as the phantom thickness increased, without significant difference in stiffness for tissue phantoms thicker than 10 mm (Fig. 5(e)).

We further measured the stiffness of phantoms with different gelatin concentrations (5, 10, and 15% w/v; phantom thickness: 10 mm; Fig. 6, Fig. S5). The slope of the acquired force-displacement curves increased with the gelatin concentration (Fig. 6(a)). For 5, 10, and 15% w/v tissue phantoms, the measured E was 18.3 ± 1.5, 25.7 ± 2.2, and 42.5 ± 1.6 kPa, respectively (Fig. 6(b)). The results were in the range of elastic moduli of physically-crosslinked gelatin phantoms measured via our published vacuum-based method [13].

Further, we used tissue phantoms to investigate whether the palpation device can profile tissues with spatially heterogenous stiffness, such as a tumor formed in tissue (Fig. 7). To this end,

an ICG-labeled cylindrical-shaped PDMS, which recapitulated a stiff nodule, was embedded at the central region of a soft 10% gelatin block (Fig. 7(a) and Fig. S6). The location of the ICG-labeled PDMS nodule was confirmed visually via near-infrared (NIR) imaging (Fig. 7(a) and Supplementary Methods). Then, the stiffness of the tissue phantom was mapped using our palpation device (Fig. 7(b) and (c)). Starting from the upper left corner of the phantom, the stiffness was measured by gently compressing the surface of the tissue mimic and recording the force and electrical signals. The stiffness map showing the elastic modulus distribution with a spatial resolution of 5 mm was generated (Fig. 7(c)). Notably, while the E values at peripheral areas of the phantom block varied between 23 and 27 kPa, there was a substantial increase in the E values (range: 38–50 kPa) at the center of the tissue phantom where the PDMS-based nodule was located, highlighting the ability of our device in accurate and quantitative localization of a stiff tissue mimic.

B. Stiffness Recording of Swine Lung and Tumor Mimic

We investigated whether our palpation device can accurately measure the elastic modulus of human-sized swine lungs that were subjected to various internal air pressures (Fig. 8). The tissue stiffness was without ventilating the lungs to minimize motion-induced measurement errors. Specifically, the intra-peak inspiratory pressure (PIP) of the lungs were adjusted to a constant level (e.g., 2, 25, and 45 cmH$_2$O) during each measurement using an Ambu bag and a pressure sensor integrated into the tracheal tubing (Fig. 8(a)). The measured E values were measured to be 9.1 ± 2.3, 16.8 ± 1.8, and 26.0 ± 3.6 kPa when the internal pressure of the lungs (PIP) was subjected to 2, 25, and 45 cmH$_2$O, respectively (Fig. 8(b)). Notably, the lung tissue stiffness increased with PIP due to changes in the tension (T) of the lung parenchymal tissue within the pleural network and alveolar septa with respect to the pressure inside the lungs [39]. The E values measured using our device were in the range reported in the literature [40], [41].

We further created a lung tumor model that mimicked the presence of small nodules in the distal regions of the lungs to determine whether our palpation device can accurately discriminate the nodules from healthy tissue (Fig. 8(c)). The lung cancer model was generated using an explanted swine lung and an ICG-labelled PDMS block as a nodule mimic (size: 2 cm; thickness: 5 mm) (Fig. 8(c)). An incision was created in the right lobe, and the nodule was placed in the subpleural region, approximately 5 mm below the pleura surface (Fig. 8(c), Fig. S7). We used the imaging module of the palpation device to visualize the location of the nodule in the subpleural region (Fig. 8(c)). The measurement probe was then moved to different regions of the lobe (distance between measured regions: ~1 cm) to evaluate the stiffness across the lung tissue near the region where the nodule mimic was implanted. Following the scanning, a stiffness map showing the distribution of the elastic modulus across the entire lobe was generated (Fig. 8(d)). Notably, the E values ranged from 9.3 to 28.3 kPa, where the stiffness of 28.3 kPa corresponded to the precise location of the nodules in
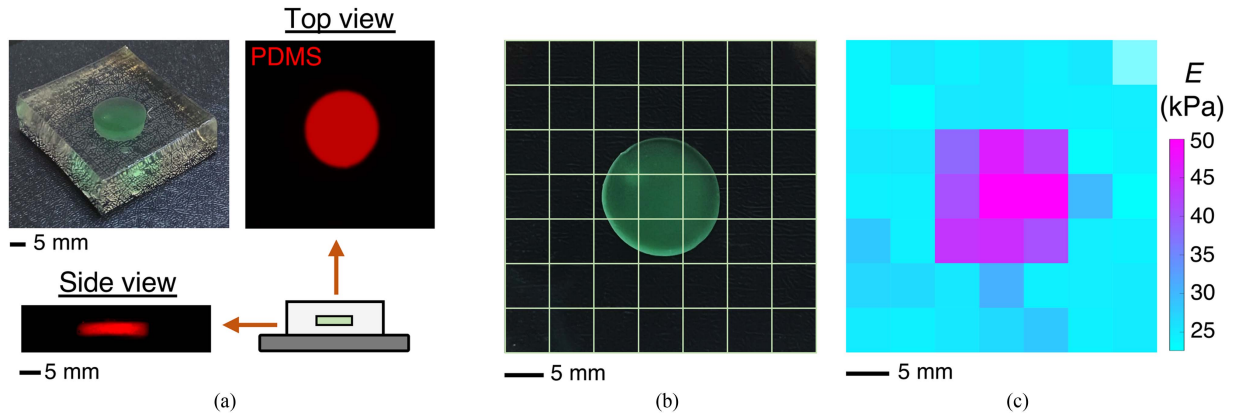
Fig. 7. Stiffness measurements of tissue phantoms with spatially heterogenous stiffness for demonstration of tumor mimic detection. (a) Images and drawing showing a cylindrical PDMS-based nodule mimic embedded in a soft hydrogel for demonstration of the nodule detection using our palpation device. The nodule mimic (diameter: 12 mm; thickness: 2.5 mm; elastic modulus: 233.3 ± 16 kPa) was labeled with near-infrared dye ICG and embedded at the center of a gelatin block (concentration: 10% w/v; length: 35 mm, width: 35 mm, thickness: 10 mm; elastic modulus: 25.7 ± 2.2 kPa). The nodule mimic was visualized in the gelatin block (red) with NIR imaging to show its location within the gelatin. (b) The tissue phantom was scanned using the palpation device with a 5-mm spatial resolution. In the image, each grid represents a spot for the stiffness measurement. (c) Two-dimensional (2D) stiffness map was obtained following discrete measurements across the phantom's surface. While the elastic moduli (E) of peripheral regions varied between 23 and 27 kPa, the E values increased to 38–50 kPa at the central region where the nodule mimic was embedded, highlighting the ability of the palpation device to detect the nodule mimic.
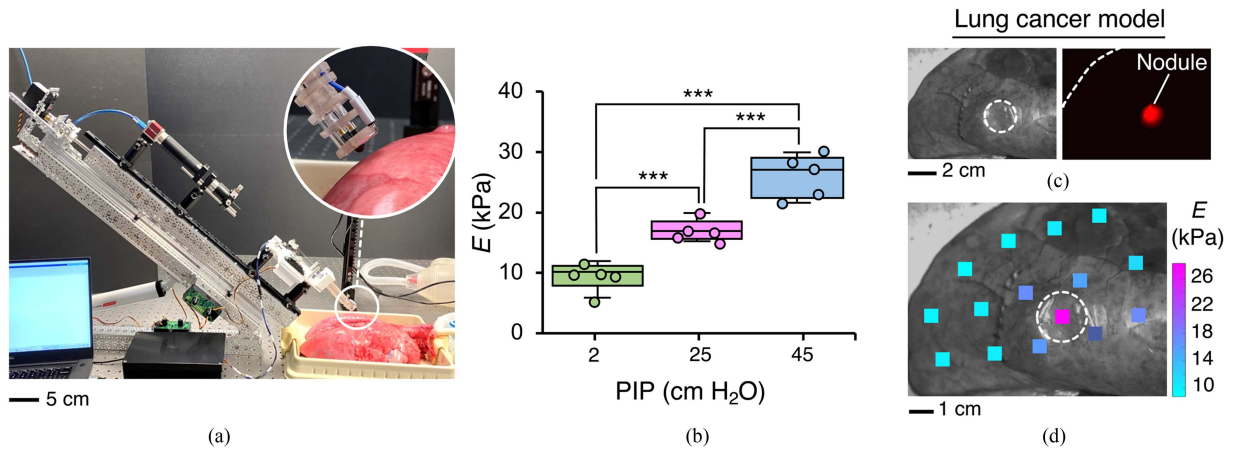

Fig. 8. Stiffness measurements of *ex vivo* swine lungs and nodule mimic detection. (a) A photograph of the measurement setup. Inset image: magnified view of the measurement probe positioned near the lung surface. (b) Elastic moduli of porcine lungs at different peak inspiratory pressure (PIP, $n = 5$). The E values increased with PIP, confirming that the tension of the lung tissue increased with PIP. The measured E values were 9.1 ± 2.3, 16.8 ± 1.8, and 26.0 ± 3.6 for 2, 25, and 45 cmH$_2$O of PIP, respectively (***p-value < 0.001). (c) Lung tumor model was created by embedding a rigid PDMS-based nodule mimic (diameter: 2 cm; thickness: 5 mm; E: 233.3 ± 16 kPa) at the depth of 5 mm in the subpleural regions. Bright-field and NIR fluorescent images of the lung lobe embedded with a nodule mimic were acquired. (d) A stiffness map of the lung cancer model showing increased stiffness near the region where tumor mimic was embedded (i.e., E: 28.3 kPa). Lower E value measured for the nodule mimic within the lung can be attributed to the presence of soft lung tissue surrounding the rigid nodule.

the lung lobe, confirming the ability of the device to locate the small nodule in the lung.

C. Stiffness Measurements of Rat and Swine Organs

We further determined the tissue stiffness of rat liver and lung, and swine heart, liver, skin, and muscle (Fig. 9 and Fig. S8). The measured E values were 2.6 ± 0.3 and 9.2 ± 0.5 kPa for rat lung (peak inspiratory pressure: 2 cmH$_2$O) and liver, respectively (Fig. 9(a)). The measured E values were 33.0 ± 5.4, 19.2 ± 2.2, 33.5 ± 8.2, and 22.6 ± 6.0 kPa, for swine heart, liver, abdominal skin, and muscle, respectively (Fig. 9(b)), and were similar to the values reported in the literature (Table S2) [42].

IV. DISCUSSIONS

The adoption and utilization of robot-assisted surgery has continued to rise, and it is anticipated to persist as technology evolves and patient outcomes improve. Given this trend, there is a growing need to develop technologies to improve surgeons' ability to access tissue health and identify pathologic lesions, such as tumors, in real-time. Current technologies, such as pre-operative localization with wires, markers, and dye are limited in their effectiveness and applicability [43], [44]. Other intra-operative imaging modalities such as ultrasound, fluorescent imaging, photoacoustic, and Raman spectroscopy have failed to have a significant clinical impact on the accuracy
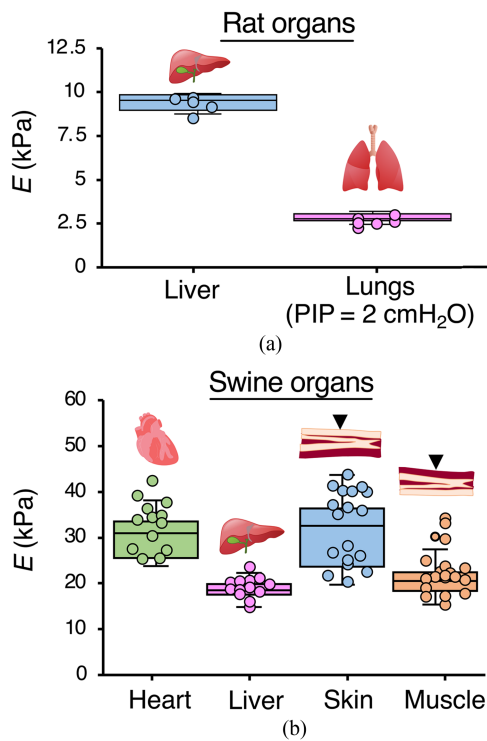
Fig. 9. Stiffness measurement of rat and swine organs using the palpation device. (a) Elastic moduli (E) of rat liver ($n = 5$) and lung ($n = 5$) were 2.6 ± 0.3 and 9.2 ± 0.5 kPa, respectively. (b) The measured E values of swine heart, liver, skin, and muscle were 33.0 ± 5.4, 19.2 ± 2.2, 33.5 ± 8.2, and 22.6 ± 6.0 kPa, respectively. The measured E values were consistent with data reported in the literature. PIP: Peak inspiratory pressure.

of localizing small tumors, due to their limited spatial resolution [45]. Inaccurate localization and delineation of tumor margins may result in either excessive or sufficient removal of tissue during tumor resection, which may necessitate re-operation [46]. During robot-assisted procedures, the surgeon may evaluate the tissue stiffness by grasping it with surgical tools and visually inspecting its response to stretch and compression. This assessment, however, is subjective and may result in tissue damage and reduced blood flow due to the lack of tactile perceptions during tissue-surgical tools contact [47]. In contrast, quantitative profiling of tissue stiffness can allow surgeons to make objective and data-driven decisions during tissue resection procedures.

To improve the precision and accuracy in detection of pathologic tissues during RMIS, we created a robotic tissue palpation device that can quantify the stiffness of tissues (Fig. 1). Our palpation device was integrated with a sensing probe, steerable catheter, a motion control module, and an optical fiber-based imaging module. The tissue stiffness measurement is achieved by gently compressing soft tissue with a rigid hemispherical indenter to deform the tissue to a specified depth (L_C). The magnitude of the force (F_C) required to deform the local tissue to correlated with L_C to estimate the tissue stiffness or elastic modulus (E). Significantly, this compression-based approach can allow intraoperative tissue stiffness assessment in real time without damaging the local tissue.

Multi-directional movements, including translational, tilting, and deflection motion of the device, were enabled by simultaneously controlling servo motors (Fig. 2). The conformable and controllable device motions facilitate the intra-operative navigation and tissue compression within a tight space, such as chest cavity. In particular, the wire-driven design of the catheter can provide dexterity, allowing the probe to apply the normal force to tissue with irregular surface topology. The majority of palpation devices reported in the literature have a limited range of motion and flexibility [20], [28], [34], [48], [49], which makes them difficult to use during robotic surgery. In contrast, our device is capable of maneuvering in confined spaces, allowing surgeons to access to the surgical targets and survey questionable tissue rapidly [50], [51]. We envision our device will be able to integrate into a standard robotic or laparoscopic device arm and be controlled by the surgeon with existing interfaces. Each scenario requires thorough considerations, such as the adaptability to clinical requirements, interoperability with other robotic systems and surgical instruments, and optimization of the device's size. Additionally, In future designs, the size of the current catheter (diameter: 20 mm) can be minimized to fit into the surgical ports used in minimally invasive and robotic surgery (diameter: 5 to 12 mm) [52].

The optical fiber imaging probe incorporated into the device allows visual monitoring of the local tissue during stiffness measurement. Notably, the imaging module can be customized to enable visualization at the cellular level, as demonstrated in our previous study [53]. By implementing a real-time image processing scheme, such as Gaussian filtering, the quality of images and videos can be substantially improved (Fig. 3, Fig. S9). Moreover, the flexibility of the imaging fiber facilitates integration into the steerable catheter. Further, the bifurcated geometry of the imaging fiber enables simultaneous illumination and imaging, with the light passing through the "transmitting bundle" to the fiber tip and the fluorescent signal passing through the "receiving bundle" into the camera. This imaging capability can be useful during intra-operative tumor resection, where surgeons can administer fluorescent molecules that can specifically label tumors to improve the accuracy of tumor identification and resection [54].

To obtain precise tissue stiffness measurements with our palpation device, it is essential to ensure that the device's distal end is positioned perpendicular to the tissue surface, allowing the generation of a normal force during the measurement. Deviation from this perpendicular alignment can result in shear forces applied to the tissue due to an angled device position, which can introduce inaccuracies in the readings. The impact of these shear forces can be particularly pronounced when dealing with tissues that have slippery surfaces, especially if the slipperiness is not consistent across the tissue surface.

Orthogonal positioning of the device with respect to the tissue surface can be achieved by ensuring that the two contact electrodes simultaneously touch the tissue surface. Minor deviations (e.g., a few angles) from perfect orthogonality may lead to negligible impact on the accuracy of the measurements.

In future design improvements, we can enhance accuracy by adding more contact electrodes, for example, four electrodes,

to the device. This increased electrode count can help ensure perpendicular tissue compression, leading to greater precision in device positioning and accurate measurements [26].

Utilizing imaging guidance can greatly assist in achieving proper orthogonal positioning of the device during the procedure. In our experiments, we ensured the probe's correct alignment with the tissue surface by monitoring its position using a camera placed adjacent to the measurement site. Likewise, in robotic surgery, incorporating a surgical camera can aid the surgeon in accurately positioning the palpation device for stiffness measurements in real-time. Furthermore, advanced imaging methods, 3D topography in particular, can be employed to assess the tissue surface's structural features, facilitating precise alignment of the device to achieve the desired orientation [55], [56], [57].

The innovative feature of the palpation device developed in the current study is the integrated contact electrodes circuit, which informs the maximum tissue deformation (Fig. 5). In our design, the deformation of tissue to a specified degree can be accurately determined through non-invasive, real-time recording of voltage via the electrodes. The current deformation measurement methods, such as optically based and computer-assisted approaches, are time-consuming and prone to errors [58]. On the other hand, a predetermined magnitude of tissue deformation can be achieved intraoperatively using our approach. Further, the deformation length can be easily customized by using a hemispheric indenter with different heights. The magnitudes of electrical voltage and current (voltage: 3.2 volts, current: 0.5 mA) used in this study, which could also be easily adjusted to different values, were within a safe and clinically relevant range (Figs. 4, 5, 6, 7, 8, and 9) [11], [59].

Despite the several advantages of the tissue palpation prototype presented in this work, some areas need to be improved. For example, the resolution of the stiffness map can be improved by applying finer discretization or using a smaller indenter. Moreover, a cylindrical nodule mimic with a constant stiffness value was used in the lung cancer model, and stiffness measurements were performed on *ex vivo* tissues. Given that tumors have different topologies and mechanical properties at various developmental stages, further studies can confirm the utility of our tissue palpation device in various *in vivo* scenarios [23]. Furthermore, the tissue phantoms and biological tissues in this study were assumed to be elastic within the applied deformation ranges. Nonlinear viscoelasticity of the tissues and its effect on stiffness measurements and localization of pathologic tissues can be studied more thoroughly to provide clear picture of the structural complexity of biological tissues [22].

V. CONCLUSION

Overall, the study highlights the potential of a novel robotic tissue palpation device as an intraoperative tool that can assess and localize pathologic tissues with altered mechanical properties, such as tumors. The quantitative data provided by the palpation device can be interpreted along with the results of other pre- and intra-operative techniques to give clearer insight of tumors location and margins to surgeons. Exciting prospects for the future of this device include even more sensitive and precise measurements through design improvements, validation of its functions through *in vivo* animal experiments, and the utilization of this innovative technology in real-world clinical settings. With these developments, robotic palpation technology may have a profound impact on tissue assessment and surgical procedures in the future.

REFERENCES

[1] B. S. Peters et al., "Review of emerging surgical robotic technology," *Surg. Endoscopy*, vol. 32, no. 4, pp. 1636–1655, Apr. 2018.

[2] V. Vitiello et al., "Emerging robotic platforms for minimally invasive surgery," *IEEE Rev. Biomed. Eng.*, vol. 6, pp. 111–126, 2013.

[3] O. M. Omisore et al., "A review on flexible robotic systems for minimally invasive surgery," *IEEE Trans. Syst., Man, Cybern., Syst.*, vol. 52, no. 1, pp. 631–644, Jan. 2022.

[4] U. Kim et al., "A surgical palpation probe with 6-axis force/torque sensing capability for minimally invasive surgery," *IEEE Trans. Ind. Electron.*, vol. 65, no. 3, pp. 2755–2765, Mar. 2018.

[5] M. K. Ibrahim et al., "Robot-assisted for medical surgery: A literature review," *AIP Conf. Proc.*, vol. 2591, no. 1, Mar. 2023, Art. no. 030008.

[6] N. Simaan, R. M. Yasin, and L. Wang, "Medical technologies and challenges of robot-assisted minimally invasive intervention and diagnostics," *Annu. Rev. Control, Robot., Auton. Syst.*, vol. 1, no. 1, pp. 465–490, May 2018.

[7] Y. Kobayashi et al., "Intraoperative real-time tissue elastography during laparoscopic hepatectomy," *Hepatobiliary Pancreatic*, vol. 20, no. 1, pp. 93–99, Jan. 2018.

[8] O. Rouvière et al., "Stiffness of benign and malignant prostate tissue measured by shear-wave elastography: A preliminary study," *Eur. Radiol.*, vol. 27, no. 5, pp. 1858–1866, May 2017.

[9] J. H. W. Distler et al., "Shared and distinct mechanisms of fibrosis," *Nature Rev. Rheumatol.*, vol. 15, no. 12, pp. 705–730, Dec. 2019.

[10] A. Abiri et al., "Artificial palpation in robotic surgery using haptic feedback," *Surg. Endoscopy*, vol. 33, no. 4, pp. 1252–1259, Apr. 2019.

[11] J. Chen et al., "Opto-electromechanical quantification of epithelial barrier function in injured and healthy airway tissues," *APL Bioeng.*, vol. 7, no. 1, pp. 016104, Mar. 2023.

[12] S. G. de Koning et al., "Tumor resection margin definitions in breast-conserving surgery: Systematic review and meta-analysis of the current literature," *Clin. Breast Cancer*, vol. 18, no. 4, pp. e595–e600, Aug. 2018.

[13] J. Chen et al., "Non-destructive vacuum-assisted measurement of lung elastic modulus," *Acta Biomaterialia*, vol. 131, pp. 370–380, Sep. 2021.

[14] T. Huseini and M. Liberman, "Commentary: Finding a needle in a haystack—Technology and innovation for precise intraoperative localization of deep-seated pulmonary nodules," *JTCVS Techn.*, vol. 5, pp. 107–108, Feb. 2021.

[15] J. F. Greenleaf, M. Fatemi, and M. Insana, "Selected methods for imaging elastic properties of biological tissues," *Annu. Rev. Biomed. Eng.*, vol. 5, pp. 57–78, 2003.

[16] H. Liu et al., "Rolling indentation probe for tissue abnormality identification during minimally invasive surgery," *IEEE Trans. Robot.*, vol. 27, no. 3, pp. 450–460, Jun. 2011.

[17] M. Li et al., "A novel tumor localization method using haptic palpation based on soft tissue probing data," in *Proc. IEEE Int. Conf. Robot. Automat.*, 2014, pp. 4188–4193.

[18] M. Li et al., "Intra-operative tumour localisation in robot-assisted minimally invasive surgery: A review," *Proc. Inst. Mech. Eng.*, vol. 228, no. 5, pp. 509–522, May 2014.

[19] E. Samur et al., "A robotic indenter for minimally invasive measurement and characterization of soft tissue response," *Med. Image Anal.*, vol. 11, no. 4, pp. 361–373, Aug. 2007.

[20] T. Li, C. Shi, and H. Ren, "A high-sensitivity tactile sensor array based on fiber bragg grating sensing for tissue palpation in minimally invasive surgery," *IEEE/ASME Trans. Mechatron.*, vol. 23, no. 5, pp. 2306–2315, May 2018.

[21] M. Beccani et al., "Wireless tissue palpation for intraoperative detection of lumps in the soft tissue," *IEEE Trans. Biomed. Eng.*, vol. 61, no. 2, pp. 353–361, Feb. 2014.

[22] J. Palacio-Torralba et al., "Quantitative diagnostics of soft tissue through viscoelastic characterization using time-based instrumented palpation," *J. Mech. Behav. Biomed. Mater.*, vol. 41, pp. 149–160, Jan. 2015.

[23] Y. Yun et al., "Palpation-based multi-tumor detection method considering moving distance for robot-assisted minimally invasive surgery," in *Proc. 42nd Annu. Int. Conf. IEEE Eng. Med. Biol. Soc.*, 2020, pp. 4899–4902.

[24] G. Tholey and J. P. Desai, "A compact and modular laparoscopic grasper with tridirectional force measurement capability," *J. Med. Devices*, vol. 2, no. 3, 2008, Art. no. 25120.

[25] H. Liu et al., "The MUSHA hand II:A multifunctional hand for robot-assisted laparoscopic surgery," *IEEE/ASME Trans. Mechatron.*, vol. 26, no. 1, pp. 393–404, Feb. 2021.

[26] B. Ahn et al., "Robotic palpation and mechanical property characterization for abnormal tissue localization," *Med. Biol. Eng. Comput.*, vol. 50, no. 9, pp. 961–971, Sep. 2012.

[27] N. Bandari, J. Dargahi, and M. Packirisamy, "Tactile sensors for minimally invasive surgery: A review of the state-of-the-art, applications, and perspectives," *IEEE Access*, vol. 8, pp. 7682–7708, 2020.

[28] P. Puangmali et al., "Miniature 3-axis distal force sensor for minimally invasive surgical palpation," *IEEE/ASME Trans. Mechatron.*, vol. 17, no. 4, pp. 646–656, Aug. 2012.

[29] C. - H. Chuang et al., "Piezoelectric tactile sensor for submucosal tumor detection in endoscopy," *Sensors Actuators A: Phys.*, vol. 244, pp. 299–309, Jun. 2016.

[30] S. Schostek et al., "Artificial tactile sensing in minimally invasive surgery - a new technical approach," *Minimally Invasive Ther. Allied Technol.*, vol. 15, no. 5, pp. 296–304, 2006.

[31] M. Jin et al., "Visual tactile sensor based on infrared controllable variable stiffness structure," *IEEE Sensors J.*, vol. 21, no. 23, pp. 27076–27083, Dec. 2021.

[32] Y. Yan and J. Pan, "Fast localization and segmentation of tissue abnormalities by autonomous robotic palpation," *IEEE Robot. Automat. Lett.*, vol. 6, no. 2, pp. 1707–1714, Apr. 2021.

[33] W. Othman et al., "Stiffness assessment and lump detection in minimally invasive surgery using in-house developed smart laparoscopic forceps," *IEEE J. Transl. Eng. Health Med.*, vol. 10, 2022, Art. no. 2500410.

[34] S. McKinley et al., "A single-use haptic palpation probe for locating subcutaneous blood vessels in robot-assisted minimally invasive surgery," in *Proc. IEEE Int. Conf. Automat. Sci. Eng.*, 2015, pp. 1151–1158.

[35] A. S. Naidu, R. V. Patel, and M. D. Naish, "Low-cost disposable tactile sensors for palpation in minimally invasive surgery," *IEEE/ASME Trans. Mechatron.*, vol. 22, no. 1, pp. 127–137, Feb. 2017.

[36] P. Scanlan et al., "Development of a novel actuator for the dynamic palpation of soft tissue for use in the assessment of prostate tissue quality," *Sensors Actuators A: Phys.*, vol. 232, pp. 310–318, Aug. 2015.

[37] E. Samur et al., "A robotic indenter for minimally invasive characterization of soft tissues," *Int. Congr. Ser.*, vol. 1281, pp. 713–718, May 2005.

[38] J. S. Wang et al., "Evaluation of the substrate effect on indentation behavior of film/substrate system," *Appl. Surf. Sci.*, vol. 256, no. 20, pp. 5998–6002, Aug. 2010.

[39] S. Andreassen et al., "The effect of tissue elastic properties and surfactant on alveolar stability," *J. Appl. Physiol.*, vol. 109, no. 5, pp. 1369–1377, 2010.

[40] X. Zhang, R. R. Kinnick, and J. F. Greenleaf, "Viscoelasticity of lung tissue with surface wave method," in *Proc. IEEE Ultrason. Symp.*, 2008, pp. 21–23.

[41] Z. Dai et al., "A model of lung parenchyma stress relaxation using fractional viscoelasticity," *Med. Eng. Phys.*, vol. 37, no. 8, pp. 752–758, Aug. 2015.

[42] S. Budday et al., "Fifty shades of brain: A review on the mechanical testing and modeling of brain tissue," *Arch. Comput. Methods Eng.*, vol. 27, no. 4, pp. 1187–1230, Sep. 2020.

[43] S. H. Chang et al., "Narrative review: Preoperative localization techniques for small lung nodules," *Curr. Challenges Thoracic Surg.*, vol. 4, Nov. 2022, Art. no. 10122021.

[44] I. Boekestijn et al., "The current status and future prospects for molecular imaging-guided precision surgery," *Cancer Imag.*, vol. 22, no. 1, Sep. 2022, Art. no. 48.

[45] I. S. Alam et al., "Emerging intraoperative imaging modalities to improve surgical precision," *Mol. Imag. Biol.*, vol. 20, no. 5, pp. 705–715, Oct. 2018.

[46] G. Tsoumakidou et al., "Image-guided marking techniques in interventional radiology: A review of current evidence," *Diagn. Interventional Imag.*, vol. 102, no. 12, pp. 699–707, Dec. 2021.

[47] K. H. Kernstine, C. A. Anderson, and A. Falabella, "Robotic lobectomy," *Operative Techn. Thoracic Cardiovasc. Surg.*, vol. 13, no. 3, pp. 204.e1–204.e23, Sep. 2008.

[48] H. Oflaz and O. Baran, "A new medical device to measure a stiffness of soft materials," *Acta Bioeng. Biomech.*, vol. 16, no. 1, pp. 125–131, 2014.

[49] I. B. Wanninayake et al., "Air-float palpation probe for tissue abnormality identification during minimally invasive surgery," *IEEE Trans. Biomed. Eng.*, vol. 60, no. 10, pp. 2735–2744, Oct. 2013.

[50] X. Hu et al., "Steerable catheters for minimally invasive surgery: A review and future directions," *Comput. Assist. Surg.*, vol. 23, no. 1, pp. 21–41, Jan. 2018.

[51] Z. Li et al., "Kinematic comparison of surgical tendon-driven manipulators and concentric tube manipulators," *Mechanism Mach. Theory*, vol. 107, pp. 148–165, Jan. 2017.

[52] A. S. Laganà et al., "Mini-laparoscopy or single-site robotic surgery in gynecology? let's think out of the box," *J. Invest. Surg.*, vol. 35, no. 2, pp. 440–441, Feb. 2022.

[53] J. Kim et al., "Controlled delivery and minimally invasive imaging of stem cells in the lung," *Sci. Rep.*, vol. 7, no. 1, Oct. 2017, Art. no. 13082.

[54] Y. - J. Lee et al., "A narrative review of fluorescence imaging in robotic-assisted surgery," *Laparoscopic Surg.*, vol. 5, 2021, Art. no. 31.

[55] N. Marahrens et al., "Towards autonomous robotic minimally invasive ultrasound scanning and vessel reconstruction on non-planar surfaces," *Front. Robot. AI*, vol. 9, 2022, Art. no. 251202.

[56] C. Zhou et al., "Ferromagnetic soft catheter robots for minimally invasive bioprinting," *Nature Commun.*, vol. 12, no. 1, Aug. 2021, Art. no. 5072.

[57] M. Unger, J. Berger, and A. Melzer, "Robot-assisted image-guided interventions," *Front. Robot. AI*, vol. 8, 2021, Art. no. 021021.

[58] L. Huang et al., "Experimental mechanical strain measurement of tissues," *PeerJ*, vol. 7, 2019, Art. no. e6545.

[59] M. Kono et al., "Design guideline for developing safe systems that apply electricity to the human body," *ACM Trans. Comput.-Hum. Interaction*, vol. 25, no. 3, 2018, Art. no. 19.